Title	Comparison of cellular architecture, axonal growth, and blood vessel formation through cell-loaded polymer scaffolds in the transected rat spinal cord
Author(s)	Madigan, Nicolas N.; Chen, Bingkun K.; Knight, Andrew M.; Rooney, Gemma E.; Sweeney, Eva; Kinnavane, Lisa; Yaszemski, Michael J.; Dockery, Peter; O'Brien, Timothy; McMahon, Siobhan S.; Windebank, Anthony J.
Publication Date	2014-08-08
Publication Information	Madigan, Nicolas N., Chen, Bingkun K., Knight, Andrew M., Rooney, Gemma E., Sweeney, Eva, Kinnavane, Lisa, Yaszemski, Michael J., Dockery, Peter, O'Brien, Timothy, McMahon, Siobhan S., Windebank, Anthony J. (2014). Comparison of Cellular Architecture, Axonal Growth, and Blood Vessel Formation Through Cell-Loaded Polymer Scaffolds in the Transected Rat Spinal Cord. Tissue Engineering Part A, 20(21-22), 2985-2997. doi: 10.1089/ten.tea.2013.0551
Publisher	Mary Ann Liebert
Link to publisher's version	https://doi.org/10.1089/ten.tea.2013.0551
Item record	http://hdl.handle.net/10379/15344
DOI	http://dx.doi.org/10.1089/ten.tea.2013.0551

Comparison of Cellular Architecture, Axonal Growth, and Blood Vessel Formation Through Cell-Loaded Polymer Scaffolds in the Transected Rat Spinal Cord

Nicolas N. Madigan, MD, PhD,[1,2] Bingkun K. Chen, MD, PhD[1], Andrew M. Knight, PhD,[1] Gemma E. Rooney, PhD,[1] Eva Sweeney,[2] Lisa Kinnavane,[2] Michael J. Yaszemski, MD, PhD,[2] Peter Dockery, PhD,[2] Timothy O'Brien MD, PhD,[2] Siobhan S. McMahon, PhD,[2] Anthony J. Windebank, MD,[1*]

[1]Department of Neurology, Mayo Clinic College of Medicine, Mayo Clinic, Rochester, MN, USA.

[2]Regenerative Medicine Institute (REMEDI), Department of Medicine, National University of Ireland, Galway, Ireland.

[3]Department of Orthopedic Surgery, Mayo Clinic College of Medicine, Mayo Clinic, Rochester, MN, USA.

ABSTRACT

The use of scaffolds in a complete transection model of spinal cord injury serves as a deconstructed model that allows for manipulation of specific variables in the microenvironment and direct observation of their effects on regeneration. In this study, multichannel polymer scaffolds were fabricated from positively charged oligo[poly(ethylene glycol)fumarate] (OPF+) hydrogel and implanted into rat spinal cords following T9 complete transection. OPF^{+} scaffold channels were loaded with either syngeneic Schwann cells or mesenchymal stem cells that have been derived from enhanced green fluorescent protein transgenic rat (eGFP-MSCs). Control scaffolds contained extracellular matrix only. The capacity of each scaffold type to influence the architecture of regenerated tissue after four weeks was examined by detailed immunohistochemistry and stereology. Astrocytosis was observed in a circumferential peripheral channel compartment. A structurally separated channel core contained scattered astrocytes, Schwann cells, eGFP-MSCs, blood vessels and regenerating axons. Schwann cells double-stained with GFAP and S-100 antibodies populated each scaffold type demonstrating migration of an immature cell phenotype into the scaffold from the animal. eGFP-MSCs survived in low numbers and were distributed in close association with blood vessels. Quantification of axonal counts demonstrated that regeneration was augmented by the presence of Schwann cells in implanted scaffolds, while eGFP-MSCs did not support axon growth. Axon regeneration was analysed in relationship to the developing channel vasculature. Methods of unbiased stereology provided physiologic estimates of blood vessel volume, length and surface area, as well as mean vessel diameter and cross sectional area for each channel type. Schwann cell channels had high numbers of small, densely

packed vessels. In contrast, the eGFP-MSC scaffold channels contained less but larger vessels. There was a positive linear correlation between axon counts and corresponding vessel length density, surface density, and volume fraction. Increased axon number also correlated with decreasing vessel diameter, implicating the importance of blood flow rate within channels. Radial diffusion distances in vessels correlated significantly to axon number as a hyperbolic function, showing a need to engineer high numbers of small vessels in parallel to improving axonal densities.

Introduction

Hydrogel polymer scaffolds can integrate combinations of therapies necessary for functional spinal cord repair [1-3]. Strategies to both promote axonal growth [4] and reduce inhibitory cues [5] will be necessary to facilitate regeneration of neural tissue through the barriers consequent to spinal cord injury (SCI) [6]. Nervous tissue regeneration may be supported by the matrix properties of the selected polymer and the architecture of the scaffold. Permissive microstructures such as pores, grooves, polymer fibres, and surface modifications may provide improved axon adherence and growth directionality [7]. Scaffolds or patterned substrates derived from natural materials such collagen [8], hyaluronic acid [9-11] agarose [12], fibrin [13], fibronectin [14], and chitosan [15, 16], have been proposed as scaffolds. Synthetic scaffolds include biodegradable hydrogels based on polyethylene glycol [17] or non-biodegradable hydrogels based on methacrylate [18]. We recently compared four different polymer types [19], demonstrating improved axonal density and accuracy of growth orientation using the positively charged hydrogel polymer oligo[poly(ethylene glycol)fumarate] (OPF^+). OPF is a polyethylene glycol (PEG)-based macromer incorporating a fumarate moiety which is photo-cross-linked to form a soft, porous biodegradable hydrogel [17]. OPF can be polymerized with monomer [2-(methacryloyloxy) ethyl]-trimethylammonium chloride (MAETAC) to produce the positively charged substrate (OPF^+). OPF^+ surface enhances neuronal cell attachment, Schwann cell migration and axonal myelination *in vitro* [20]

Cell implantation within scaffolds remains a foundation for combination therapies, utilizing supportive properties innate to the cell line, as well as genetic modification [21] to deliver neurotrophic molecules [22] or targeted molecular

therapies [23, 24]. Schwann cells have been consistently shown to be one of the most effective therapeutic cell types in regeneration after experimental spinal cord injury [25, 26]. These cells reduce the size of spinal cysts, remyelinate axons [27] and improve functional recovery in spinal cord injury [28]. Schwann cells have also been shown to produce a number of growth factors that initiate and support the growth of axons, and to express cell adhesion molecules on their surface for axon guidance [29]. Autologous schwann cells have recently been introduced as a potential therapy in patients with spinal cord injury.

Mesenchymal stem cells (MSCs) in spinal cord injury have also been shown to enhance axonal regeneration and promote functional recovery in animal models [30], by means of trophic effects and tissue-sparing immunomodulation [31]. MSCs may provide both a cellular substrate and a source of secreted growth factors [32]. In central nervous system (CNS) healing, MSCs have been shown to secrete vascular endothelial growth factor, nerve growth factor, and brain-derived neurotrophic factor [33]. They increase angiogenesis, and stimulate regeneration via glial-axonal remodelling [34]. Neurogenesis and synaptogenesis may occur from resident neural stem cells [35] that are stimulated by factors secreted by implanted mesenchymal stem cells. MSCs may also supply secreted signals for the inhibition of scar formation and apoptosis [36]. MSC trophism is likely to be of greater significance for CNS tissue repair than differentiation of the cell towards nervous system phenotypes *in situ* [37]. For example, neurally-differentiated MSCs lose their neuronal phenotype upon implantation [38]. We similarly have proposed that MSCs do not differentiate into neurons or neural support cells upon direct implantation into the spinal cord [39, 40].

We have recently published controlled analyses of factors influencing axonal regeneration through multichannel scaffolds, including the cell type (Schwann cells

compared with neural stem cells [41]), and scaffold channel size [42]. Schwann cells performed better than MSCs in supporting axonal growth when implanted in OPF+ scaffolds [43]. This difference appeared to be related to blood vessel formation within the channels of the scaffolds. In that study, there were less capillaries but more axons in Schwann cell-loaded scaffolds compared with those containing MSCs. Treatment with cyclic-AMP was associated with an increase in axonal number and a decrease in capillary number [43].

In the present study, multichannel OPF^{+} scaffolds were loaded with either Schwann cells or MSCs from the bone marrow of transgenic rats with expression of the enhanced green fluorescent protein (eGFP-MSCs). The cellular composition of the scaffold channels and a detailed stereological analysis of neovascular morphology suggests a strong relationship between vessel size, number and distribution and axonal regeneration.

Materials and Methods

Cell isolation and characterization

Rat MSC primary cultures were obtained from femur and tibia bone marrow, as previously described [44] from wild type (wt) and enhanced Green Fluorescent Protein (eGFP)-transgenic Sprague Dawley (SD) animals (CZ-004 [SD TgN(act-EGFP) OsbCZ-004], Genome Information Research Center, Osaka University, Japan, n=18). The capacity for eGFP-MSC cultures to differentiate into adipocyte, osteocyte [45], and chondrocyte [46] lineages was assessed as we have previously described [44]. Rat Schwann cells were cultured from the sciatic nerves of two to five day old newborn pups as we have described [19, 41].

Flow cytometry analysis

eGFP-MSCs were characterized as previously described (38, 43). They were fixed in phosphate buffered saline (PBS) with 4% paraformaldehyde and incubated with primary antibodies to CD90, CD11b/c (mouse anti-rat, 1:200) (Biolegend, San Diego, CA), CD73 (ecto 5' nucleosidase) (mouse anti-rat, 1:100), CD45 (mouse anti-rat, 1:200), CD71 (Ox-26) (mouse anti-rat, 1:100), and CD172 (Ox-41, Signal Regulatory Protein (SIRP)) (mouse anti-rat, 1:100) (BD Biosciences, San Jose CA). Goat-anti mouse IgG (H+L) secondary antibody conjugated to AlexaFluor® 647–R-phycoerythrin (PE) (Invitrogen) was used at a dilution of 1:100. FACS analysis for eGFP and PE signal was performed on 50,000 events using FACS Calibur apparatus (Becton-Dickinson, Franklin Lakes NJ). Controls included cells only, cells with secondary antibody only, isotype control, and eGFP positive and negative fluorescent controls.

OPF^+ scaffold fabrication

OPF macromer was synthesized as a condensation reaction between poly(ethylene glycol) (PEG) and triethyamine [47] and dissolved in deionized water containing 0.05% (w/w) of photoinitiator (Irgacure 2959, Ciba-Specialty Chemicals) and 0.3 g of the cross-linking reagent N-vinyl pyrrolidinone (NVP). OPF was chemically modified at 20% w/w with the positively charged monomer [2-(methacryloyloxy) ethyl]-trimethylammonium chloride (MAETAC) (80% wt in water, Sigma-Aldrich) [20]. MAETAC is a bifunctional molecule containing both a pH-independent cationic head (quaternary ammonium) and a reactive methacryloyl group that copolymerizes with the fumarate group of the OPF. OPF^+ hydrogel scaffolds were fabricated [19] by mold injection of liquid polymer, cast over seven parallel wires of 290 μm diameter and polymerized by exposure to UV light (365 nm) at an intensity of 8 mW/cm^2 (Black-Ray Model 100AP). Individual scaffolds were cut into two millimeter lengths and sterilized prior to cell loading by immersion in serial dilutions of ethanol.

OPF^+ scaffold cell loading and surgical implantation

eGFP-MSC or Schwann cell cultures were resuspended in undiluted Matrigel™ (BD Biosciences) at a density of 50,000 cells/μL and loaded to 238,000 cells per scaffold (34,000 cells per channel). Scaffolds were loaded with Matrigel alone in control animals. All surgical and care procedures involving animals were approved by the Institutional Animal Care and Use Committee (IACUC) at the Mayo Clinic, Rochester MN USA, in accordance with the National Institute of Health, and the Institute for Laboratory Animal Research (ILAR) within the National Academy of

Sciences [48]. Surgical materials and full methodology was as we have previously described [19]. Laminectomy through the T8-T10 level, T9 transection and scaffold implantation was performed on female Sprague Dawley rats weighing 230-250 grams (Harlan Laboratories, Madison WI). Hindlimb locomotor function was assessed by means of the Basso, Beattie and Bresnahan (BBB) rating scale [49], at 2 weeks and then at 4 weeks immediately prior to tissue harvesting. Animals were sacrificed following deep anaesthesia by transcardial perfusion with 4% paraformaldehyde in PBS. The scaffold and surrounding cord was dissected free, fixed and embedded in paraffin.

Antibodies and immunohistochemistry

Primary antibodies were used against Glial Fibrillary Acid Protein (GFAP) (Rabbit anti-rat, 1:100, Dako, Carpinteria CA USA) [50, 51], S-100 antigen (mouse anti-rat, 1:300, Biogenex San Ramon CA USA) and axon neurofilament protein (mouse anti-rat monoclonal antibody (Dako, 1:50). Blood vessels were identified with primary antibody to Collagen IV (polyclonal rabbit IgG, 1:300, Abcam, Cambridge England) [52, 53]. Secondary antibodies included AlexaFluor™ 546 anti-rabbit IgG (1:100, Invitrogen Molecular Probes, Dun Laoghaire Ireland) (GFAP); IgG-linked FITC secondary label (1:100, Millipore Chemicon, Carrigtwohill Ireland) [54] and Cy-5 linked anti-mouse IgG secondary (1:100, Millipore Chemicon) (S-100 and Collagen IV); and anti-mouse IgG biotinylated secondary antibody (1:100, Dako) [55] (Neurofilament).

Rehydrated tissue sections were permeabolized in PBS with 0.4% Triton X-100. Slides were immersed in citrate buffer (10mM sodium citrate, 0.05% Tween 20, pH 6.0) preheated to 96ºC for antigen retrieval. Sections were incubated with primary

antibody in a humidified slide chamber overnight at 4ºC followed by serial washing (PBS with 0.1% Triton X-100) and application of secondary antibody. Antibody-conjugated Horseradish Peroxidase was bound to Streptavidin (ExtrAvidin-Peroxidase™, Sigma-Aldrich), with 3,3'-diaminobenzidine (DAB) as a tertiary chromogen.

Microscopy

Chromogen-stained channels were observed with a Leica DM1000 Upright Fluorescence Microscope. Fluorescent imaging was acquired with an Olympus IX81 Inverted Structured Light Microscope. Z-Stacked images were compiled from an 8 micron thickness with slices of 0.5 microns using an Optigrid structured light device. An Olympus IX81 Inverted Microscope with a Yokogawa CSU-X1 Spinning Disk Unit was used for eGFP and Cy-5 imaging.

Image analysis

Acquired images were analyzed using the NIH software, ImageJ (http://rsbweb.nih.gov/ij/download.html). Color channels were split into separate images, converted to greyscale, and an intensity threshold level was set for each stain which was kept constant. Each image was then converted to a 1 bit black and white image. For area calculations, the length (in pixels) of a graticule division was calibrated into the software, having imaged the graticule on the same microscope and at the same magnification as the image being analyzed. The area of the number of pixels making up the stained area is presented as a proportion of the number of pixels comprising the total channel area. Statistical analysis was done as a comparison of

means with Kruskal-Wallis ANOVA and a Dunn's multiple comparison of means post test.

Axon counting

Axons identified by neurofilament staining were counted using 40x and 100x objective lenses at quarter length intervals through the scaffold from the rostral scaffold-cord interface [19, 41, 42]. The Kruskal–Wallis test (nonparametric ANOVA) was used determine significant differences in median axonal counts between the three animal groups.

Stereology for blood vessel quantification

An unbiased stereological approach [56, 57] was used to calculate estimates of volume fraction (Vv), length density (Lv) and surface density (Sv) of blood vessels within each channel at quarter length intervals through the scaffold. The volume fraction (Vv) represented the proportion of each unit volume in the reference channel space occupied by a vessel structure. A simple point grid was overlaid onto the channel image field in a random orientation. The number points overlaying a vessel feature was counted as a proportion of the total number of points found to be within the reference space. The volume fraction was calculated as the total sum of feature points divided by the total sum of reference points,

$$Vv(Y, ref) = \frac{\sum_{i=1}^{m} P(Y)i}{\sum_{i=1}^{m} P(ref)i}$$

where *Y* is the vessel feature, *ref* is the channel surface, *m* is the number of fields analysed, and *i* is the number of point intersections.

The length density (Lv) represented the combined length of vessel structures embedded within a channel section. A counting frame grid was laid over the channel image in a random orientation. The area of the counting frame was associated with a central point, used to measure the reference volume. A vessel was counted if it fell either fully within the framed area or lay partially outside and overlapped with the 'acceptance lines' making up the top horizontal and right hand vertical boundary of the frame. Any vessel that overlapped the 'forbidden lines' (bottom horizontal and left-hand vertical boundary), or fell outside of the frame area was not counted. The length density was calculated as the ratio of the sum of grid-vessel intersections (i) to the sum of points falling in the reference channel space over a given field number (n),

$$Lv(Y, ref) = 2 \bullet \frac{\sum_{i=1}^{n} Q_i}{a/f \bullet \sum_{i=1}^{n} P_i}$$

where Q is the number of vessel profiles correctly sampled by the frame, P is the number of frame-associated points, and a/f is the area of the frame at the final magnification (3,600 μm^2).

The surface density (Sv) of the vessels represented the surface area of blood vessel features per volume of the reference space. A series of linear test probes associated with a reference point was used. The Sv was calculated as twice the sum of number the line-vessel intersections in inverse proportion to the sum of points striking the channel surface over a given field number (n), when the length of the line associated with the reference point (l/p) is known at the final magnification:

$$Sv(Y,ref) = \frac{2 \bullet \sum_{i=1}^{n} I_i}{l / p \bullet \sum_{i=1}^{n} P_i}$$

Physiologic parameters derived from volume fractions

Anatomical estimates V(Y) for blood vessel volume, length and surface area in scaffold channel sections were calculated from the volume fraction estimates. The relationship of total volume was determined by:

$$V(Y) = V(ref) \bullet Vv(Y,ref)$$

The average channel volume V (ref) was calculated from the mean channel area at the corresponding scaffold quarter interval multiplied the approximate thickness of the tissue section.

Mean vessel diameter, cross-sectional area and radial diffusion distance were derived from proportions of volume fraction, length density and surface density [58]. The mean vessel diameter was calculated from the ratio of surface to length density, according to the equation:

$$\bar{d} = \frac{Sv}{Lv\pi}$$

The mean cross-sectional area was calculated from all three stereologic estimates and derived from the diameter calculation, as being

$$\bar{a} = \frac{Vv}{Lv} \frac{\pi d^2}{4}$$

Length density applies inversely to the radial diffusion distance, a robust indication of a cylindrical zone of diffusion around the vessel wall [58]. This parameter was calculated from Lv estimates according to the equation:

$$r(diff) = \frac{1}{\sqrt{\pi \bullet Lv}}$$

Correlations between axon number and vessel stereology estimates

Data pairs (median axon number and volume fraction estimates) were obtained from the same animal, and from the same quarter length through each scaffold, in Matrigel and Schwann cell groups. [Statistical correlation was calculated using GraphPad 5 software, assuming a non-parametric correlation yielding Spearman r coefficients and P-values by two-tailed analysis.

Results

OPF+ scaffold implantation and regenerated tissue architecture

Positively charged oligo (poly(ethylene glycol) fumarate) (OPF+) [20] hydrogel scaffolds were fabricated by injection molding and loaded with control Matrigel™, Schwann cells or eGFP-MSCs suspended in Matrigel™ at a density of 50,000 cells per μl (Figure 1A). The cell population of eGFP-MSC cultures was homogeneously $eGFP^+/CD90^+$, $eGFP^+/CD71^+$, $eGFP^+/CD172^+$ by surface marker FACS analysis, but heterogeneous for CD73 positivity. No marker expression was seen for leukocyte (CD45) or macrophage (CD11b/c) cell types.

Cell-loaded and control scaffolds were surgically implanted between the rostral and caudal ends of complete spinal cord transections at the level T9 in 10 control, 8 SC and 10 MSC animals. Post-operative animal mortality was 10% for the control group, 25% for the SC group, 33% for the MSC group, with an overall mortality of 20%. Animals were scored for improvements in hind limb motor function according to the BBB scoring system, at 2 and 4 weeks post-operatively. Scores were consistent with complete post-operative paraplegia and animals demonstrated no significant functional recovery of motor function.

Animals were sacrificed 4 weeks after scaffold implantation. With the spinal cord dissected free, the scaffolds were seen to be well-aligned and fully integrated into transected ends of the cord, with scarring evident at the transition areas (Figure 1B). Channels of regenerated tissue were seen to extend through the length of the translucent hydrogel, and were preserved in their orientation following sectioning (Figure 1C).

The cellular architecture of scaffold channels in each of the animal groups was assessed at quarter length intervals with hematoxylin and eosin staining. All channels

were highly cellular and without areas of gross tissue necrosis. An inner core tissue type could be histologically distinguished from an outer circumferential layer extending to the channel wall. Using eosin autofluorescence[59], inner and outer channel compartments were seen to be divided by a ring of brightly fluorescent stranding (Figure 1 D-F). Multinuclear cells were seen at the channel interfaces with the polymer. In the Schwann cell channel (Figure 1E), the demarcation between tissue comprising the core and periphery was abrupt. In the eGFP-MSC channel (Figure 1F), the distribution of tissue was primarily in relation to the prominent vasculature in the core.

Quantification of the cellular composition in scaffold channel compartments

GFAP positive cells uniformly lined the inner surface of the polymer channel wall in each animal group. In the channel core, GFAP staining was isolated to individual cells or clusters and often co-localized with S-100 staining.(Figure 2 A-C). eGFP-MSCs were present at four weeks post implantation at a low percentage compared to the implantation volume (Figure 2 E-F). eGFP-MSCs localized to the central core, in proximity to vessel structures. High power imaging verified eGFP-MSC cellularity (Figure 2F).

The proportional area occupied by S-100, GFAP positive and eGFP cells in a given channel was calculated using ImageJ analysis software (Figure 3A). A significantly higher percentage of GFAP staining was measured within Matrigel filled channels (30.19 +/- 1.5 %) when compared to eGFP-MSC (19.15 +/- 2.5%) and SC filled channels (17.10 +/-1.28%), $p<0.0001$. There were no significant differences between Matrigel (5.32 +/- 0.37%), Schwann cell (7.31 +/-0.77%) and eGFP-MSC

(10.07 +/- 1.03%) with regard to the proportion of S-100 positive staining. Surviving MSCs comprised 9.81 +/- 0.98 % of the channel area.

Quantification of axon numbers showed significantly more axons regenerating in the Schwann cell group (Figure 3). The median number of regenerating axons at each quarter level was 270 axons in control animals compared to 1313 in the Schwann cell group ($p<0.01$) and 12 axons in the eGFP-MSC group ($p<0.001$), (n=18).

Axon number and blood vessel fraction correlations

Axons stained with antibody to Neurofilament protein (Figure 4 A-C) and blood vessels identified with antibody to Collagen IV (Figure 4 D-F), both were confined to the central channel core. An unbiased, stereologic approach was taken to estimate the volume fraction (Vv), length density (Lv) and surface density (Sv) of vessel structures. Physiologic estimates for each channel section were calculated by correlating the fractional volumes with each channel section volume. In Matrigel channels, the mean blood vessel volume (V) (Figure 5A) was 28,770 +/- 2894 μm^3, significantly less than both the Schwann cell channel vessel volume (131,688 +/- 15,399 μm^3, $p<0.01$) and the eGFP-MSC vessel volume (161,349 +/- 11,898 μm^3, $p<0.001$). No significance difference was seen in vessels volume between the Schwann cell and MSC channel.

The mean total vessel length (L) (Figure 5B) in Schwann cell channel sections was significantly longer (1175 +/- 147 μm,), than Matrigel (412 +/- 41 mm) ($p<0.001$) and MSC channels (564 +/- 44 mm) ($p<0.001$). The vessel surface areas (S) (Figure 5C) in Schwann cell (20,404 +/- 2231 μm^2) and MSC (13,508 +/- 819 μm^2) channels both were increased over the vessel surface area in Matrigel (7,875+/- 662 μm^2) channels ($p<0.001$ and $p<0.01$ respectively).

Mean vessel diameter was derived from the fractional estimates based upon the ratio of surface to length density. The mean diameter of MSC vessels was 8.11 +/- 0.67 μm, of significantly higher caliber than Schwann cell vessels (4.67 +/- 0.44 μm, $p<0.001$). Mean vessel cross-sectional area (Figure 5D) in the MSC group also exceeded the other two groups, measuring 20,283 +/- 5141 μm^2 compared with the Schwann cell (2392+/- 545 μm^2) and Matrigel groups (3120 +/- 883 μm^2) ($p<0.001$). The radial diffusion coefficient is a robust, stereologic measure of a cylindrical zone of diffusion around a blood vessel, calculated as the inverse function of the length density [58]. The diffusion distance for Schwann cell vessels was 198.7 +/- 16.41 mm^2 ($p<0.001$) compared to 884.0 +/- 97.6 mm^2 in Matrigel channels and 498.8 +/- 35.5 mm^2 (Figure 5E).

Significant linear correlations were seen between the axon counts and the corresponding vessel length density (Spearman $r = 0.7852$, $p<0.0001$), vessel surface density (Spearman $r = 0.7719$, $p<0.0001$), vessel volume fraction (Spearman $r = 0.6862$, $p<0.0001$) and the mean vessel diameter (Spearmann $r = - 0.4635$, $p = 0.0113$). There was a statistically significant hyperbolic relationship between axon number and vessel radial diffusion distance (Figure 5F; Spearmann r of -0.7852 $p<0.0001$).

DISCUSSION

OPF^+ scaffold channels were seen to be highly cellular, viable environments having separate central core and peripheral compartments. Scaffold channels demonstrated this similarity in their overall architecture regardless of the animal group. Our previous studies have demonstrated that the type of polymer significantly influences the core/peripheral morphology, in that polymers supporting the most clearly demarcated core best supported axonal regeneration [19]. The channel periphery was shown to uniformly stain with antibodies against the astrocyte marker GFAP. As reactive astrocytosis is a primary cellular event in the injury response, migrating astrocytes may preferentially have lined the positively charged channel wall. A significantly higher proportion of channel area was occupied by GFAP positive cells in the Matrigel group. The result likely reflects the relative availability of space within the Matrigel channel for endogenous cell migration. Sharply demarcated transitions between the astrocyte peripheral zone and central core and were characteristic of the Schwann cell channels in our study. Similar boundaries between astrocytes and transplanted Schwann cells have been observed in other studies. *In vivo* [60] and *in vitro* [61], Schwann cells are actively excluded from areas occupied by astrocytes.

The molecular components and functional significance of boundary formation in OPF^+ scaffold channels is not yet known. In other models, the number of astrocytes expressing chondroitin sulfate proteoglycans is increased in the presence of SCs in co-culture [62]. Aggregan produced by astrocytes inhibited Schwann cell motility on monolayers, while motility could be improved with RNA interference or glycosaminoglycan side chain digestion [63]. Schwann cell conditioned media was

sufficient to induce astrocyte hypertrophy, implicating a secreted factor, likely to be a fibroblast-growth factor family member on the basis of FGF ligand and receptor antibody studies [64]. Genetic upregulation of surface integrins could facilitate Schwann cell migration and functional integration into the astrocytic environment of the injured cord [65-67]. Regarding function, compartmental boundaries in the CNS including the delineation of segments, developing midlines, tract nuclei, functional columns, and discrete axonal arcs or pathways are demarcated by astrocytes. Increased GFAP staining has been observed in developmental boundaries such as the thalamic nuclei, and barrel cortical structures [68]. The extracellular matrix demarcating these boundaries is laid down by radial astrocytes and is rich in J1/tenascin glycoprotein. Spatial and temporal distributions of tenascin during development also suggest a role in the guidance of neurons within functional patterns [69]. These 'glial cordones' may be dynamic entities of specialized glia secreting glycoconjugates as mixtures of glycoproteins, glycolipids, and glycosaminoglycans, and which disappear after stable synaptic formation [70].

Axonal regeneration within the core area of scaffold channels was best supported by Schwann cells, and therefore by means of a hybrid environment of spinal cord and peripheral nervous system cellular elements. Augmentation of the peripheral elements by pre-loading scaffolds with Schwann cells may improve the efficiency of axonal growth. The result is consistent with our previous observations comparing axonal regeneration in Schwann cell and neural stem cell-loaded scaffold channels [41]. The proportion of channel area occupied by S-100 positive staining at four weeks in our current study however was not statistically different across the three animal, including the Matrigel only group which had no transplanted cells. A low proportion of channel area (less than 10 %) in our model was occupied by a

$GFAP^+/S\text{-}100^+$ cell type at four weeks. S-100 positive cells seen within the channels migrated into the scaffold, while the majority of implanted cells in our study did not survive. These cells stained with both GFAP and S-100, which raises the possibility that they are either an immature astrocyte [71] or an immature Schwann cell [72] phenotype. We have previously shown by electron microscopy that Schwann cells are present and actively myelinate regenerating axons within scaffold channels [27]. Schwann cells migrate in and de-differentiate to an immature phenotype in other complete transection models [73], regressing from mature $P0^+$ to $P0^-/p75^+$ cells which proliferate in the lesion and then gradually re-acquire $P0^+$ maturity.

Peripheral nerve Schwann cells have long been known to freely migrate into the injured cord [74]. Here they may contribute to endogenous healing by associating with injured axons and remyelinating fibres within the lesion. In contusion injuries, the cystic cavities became partially filled with nerve fibers and associated Schwann cells [75]. Mechanisms accounting the loss of implanted cells may include the robust immune response [76], poor vascularization and gas exchange [77], and production of cytotoxic nitrite and lipid free radicals within the anoxic environment [78, 79]. Cell stress given the transition from a nutrient rich culture into the hostile injury environment may also contribute to cell death [80]. That a high proportion of implanted Schwann cells die within the transplant environment has been similarly shown in a contusion model [81], where the proportion of Schwann cells present within the injury epicenter at 3 weeks post transplantation fell to 22.4 +/- 4.3 %. We would anticipate higher rates of death in a scaffold model, given that the channel environment would be more anoxic than within the intact, injured cord.

MSCs survived in implanted OPF^+ scaffolds in equally sparse numbers within the channel core area by eGFP fluorescence at 4 weeks. Pretreatment of scaffolds with

eGFP-MSC loading did not support axonal regeneration to any significant extent. This result is not in keeping with the majority of other studies using MSC transplantation techniques in spinal cord injury. Since the first described MSC engraftments into the injured cord [82], some 17 other *in vivo* animal studies have followed [30]. The majority of studies have combined a weight-impactor contusion injury in the rat thoracic followed by direct injection of cultured MSCs into the substance of the cord lesion [82-85] either at the time of the injury of or within 7 days. Cells have also been injected into the rostral and caudal tissue adjacent to the lesion in graded contusion injuries [86]. In one series [87], cell injection was delayed until 3 months post injury and the animals were followed out to 1 year [88]. Histologic endpoints have included successful MSC engraftment, remyelination, reduced cavity formation, cell bundle or bridge formation facilitating axonal regeneration, and enhanced Schwann cell migration into the wound. Where functional assessments were done, outcomes included statistical significance of improved BBB scores, increased axonal conduction velocity, improved exploratory rearing behavior, and sensory sensitivity to thermal stimuli.

Few studies however have used polymeric delivery of MSCs. MSCs seeded onto methylacrylate derivatives have been implanted into a cord hemisection model [89]. A reduction in lesion size was noted, along with higher scores in BBB testing and faster recovery of sensitivity in hind limbs. MSC-seeded scaffolds were also used in bridging a chronic injury, whereby the scaffold was implanted 5 weeks after a balloon compression injury [90] and behavioral testing up to 6 months post implantation demonstrated functional improvements. The hydrogels were infiltrated with axons which were myelinated with Schwann cells. Blood vessels and astrocytes also grew inside the implant. MSCs were reported to be present within the hydrogels

5 months after implantation. Our studies [43] are among the few studies that have used a complete transection model for the polymeric delivery of MSCs. Zeng *et al* [91] have used a collagen-gelatin sponge covered by a thin film of PLGA and seeded with MSCs for implantation into a transection model with primary endpoints of fibronectin deposition and angiogenesis. Our results may demonstrate a necessity for implanted MSCs to integrate with intact nervous tissue in proximity to the injured area.

That MSCs likely represent subpopulations of pericytes [92] [93], is a concept that connects immune and vascular functions implicated in tissue repair via granulation tissue formation [94]. Pericytes from various adult and fetal tissues have also shown expression of classically MSC-type markers, CD44, CD73, CD90 and CD105 [95]. Populations of pericytes may in addition have a neuroectodermal origin, derived from Sox1+ neuroepithelial/neuro crest cells [96], an observation that may explain the presence of nerve growth factor receptors on bone marrow MSCs, the potential for MSC neuro-differentiation, and cell tolerance within the CNS environment. Pericytes exist in the brain and retina [97], at higher density than in any other organ [98]. Here the cells may function in the stabilization and maturation of the neurovascular system as well as the blood brain barrier. Brain pericytes also have been shown to possess pluripotential activity, and are recruited at times of ischaemic injury[99]. That brain pericytes can contribute to CNS regeneration is in evidence, where the cell type gave rise to neurons and glial cells in the subgranular zone of the dentate gyrus in monkeys following ischemia [100]. Neurogenesis and angiogenesis may be linked through vascular production of stromal-derived factor 1 (SDF1) and angiopoietin 1 (Ang1). These factors can promote neuroblast migration and

behavioral recovery [101] in addition to growth and maturation of the vasculature [102].

MSC channels in our study however did not support axonal growth despite appearing to be highly vascular. Matrigel channels, which minimally supported axonal growth, were seen to be relatively avascular compared to Schwann cell and MSC channels. In Schwann cell channels, high numbers of small diameter vessels were observed, contributing to total vessel lengths of over 1 mm per channel section, twice the total length density seen Matrigel and MSC channels. Schwann cell channel vessels maintained a blood volume and surface area estimates to comparable MSC channels, by virtue of high numbers of small vessels. MSC channels maintained their blood supply by means of fewer numbers vessels of larger calibre. Such observations may further implicate the importance of blood flow rate and the relative success of axonal regeneration, with slow flow predicted through larger diameter vessels formed in MSC channels, and relatively higher flow through higher numbers of tighter vessels in the Schwann cell channel. As such, a significant correlation was shown between decreasing vessel diameter and increasing axon numbers in our study.

Primary fractional estimates of increased length volume, surface density and volume fraction also correlated significantly to increased axon number. The tightest correlation seen (Spearman $r = 0.7852$, $p<0.0001$) was between axon number and the length volume. The length volume is of particular physiologic importance as it relates to the radial diffusion distance, the measure of a cylindrical space of tissue around the vessel that will be influenced by diffusion. Of the three channel types, Matrigel demonstrated the highest radial diffusion distances (up to 800 μm) followed by MSC vessels (600 μm). Vessels in Schwann cell channels had distances of around 200 μm. The radial diffusion distances in human spinal cord grey and white matter have been

calculated in tissue sections obtained from 4 cadaver donors [58]. The values were between 15 and 20 μm in both regions, slightly higher in white matter than grey, and importantly were seen to be highly conserved across the 4 individuals. The coefficient of variance ranged between 3.3 and 5.6%. Conservation of neurovascular parameters in turn applies something of importance for species evolution and survival. Here we have shown the relationship between radial diffusion distances to correlate mathematically with axon numbers as a hyperbolic function. In order to achieve physiologic levels axon numbers, there is equal need to improve overall vessel length densities in tissue-engineered spinal cord. Improved axonal growth may depend upon higher numbers of small caliber vessels that provide a close and redundant proximity to the nutrient and oxygen supply.

In conclusion, histologic analysis of the tissue architecture formed after four weeks within OPF+ scaffold channels demonstrated established astrocytosis in a circumferential peripheral channel compartment. A structurally separate channel core contained scattered astrocytes, Schwann cells, eGFP-MSCs, blood vessels and regenerating axons. Axonal counts were augmented by the presence of Schwann cells despite a high proportion of transplanted cell death. MSCs placed in scaffolds also survived at a low rate but did not support axon growth to any extent. The low survival rate of both cell types at four weeks contrasts with the dramatic effects on axon number and vessel morphometry. The engrafted cells therefore significantly influenced the microenvironment at an early point and with a longer lasting effect on regeneration. MSCs influenced the formation of vascular elements that were unique. Whereas Schwann cell channels had high numbers of small, densely packed vessels, infrequent and large vessels dominated the structure of MSC scaffold channels. Increased axon counts correlated to higher vessel length and surface density, and with

decreasing vessel diameter, implicating the importance of blood flow rate in channels. Radial diffusion distances in vessels correlated significantly to axon number as a hyperbolic function. There is a necessity engineer higher numbers of small vessels in parallel to improving axonal densities to achieve physiologic relevance and restored neurologic function. Future studies will need to be directed towards understanding early cellular interactions after scaffold implantation and how these may be directed towards increasing vascularity with physiologic characteristics that support regeneration.

Acknowledgements

The authors gratefully acknowledge the expert technical assistance of LouAnn Gross and Jarred Nesbitt.

REFERENCES

1. Oudega, M., Bradbury, E.J., and Ramer, M.S. Combination therapies. Handbook of clinical neurology / edited by P.J. Vinken and G.W. Bruyn, 2012. **109**: p. 617-36.
2. Garcia-Alias, G., Petrosyan, H.A., Schnell, L., Horner, P.J., Bowers, W.J., Mendell, L.M., Fawcett, J.W., and Arvanian, V.L. Chondroitinase ABC combined with neurotrophin NT-3 secretion and NR2D expression promotes axonal plasticity and functional recovery in rats with lateral hemisection of the spinal cord. J Neurosci, 2011. **31**(49): p. 17788-99.
3. Kadoya, K., Tsukada, S., Lu, P., Coppola, G., Geschwind, D., Filbin, M.T., Blesch, A., and Tuszynski, M.H. Combined intrinsic and extrinsic neuronal mechanisms facilitate bridging axonal regeneration one year after spinal cord injury. Neuron, 2009. **64**(2): p. 165-72.
4. Lu, P., Blesch, A., Graham, L., Wang, Y., Samara, R., Banos, K., Haringer, V., Havton, L., Weishaupt, N., Bennett, D., Fouad, K., and Tuszynski, M.H. Motor axonal regeneration after partial and complete spinal cord transection. J Neurosci, 2012. **32**(24): p. 8208-18.
5. Hyatt, A.J., Wang, D., Kwok, J.C., Fawcett, J.W., and Martin, K.R. Controlled release of chondroitinase ABC from fibrin gel reduces the level of inhibitory glycosaminoglycan chains in lesioned spinal cord. J Control Release, 2010. **147**(1): p. 24-9.
6. McDonald, J.W. and Sadowsky, C. Spinal-cord injury. Lancet, 2002. **359**(9304): p. 417-25.
7. Madigan, N.N., McMahon, S., O'Brien, T., Yaszemski, M.J., and Windebank, A.J. Current tissue engineering and novel therapeutic approaches to axonal

regeneration following spinal cord injury using polymer scaffolds. Respir Physiol Neurobiol, 2009. **169**(2): p. 183-99.

8. Yao, L., Damodaran, G., Nikolskaya, N., Gorman, A.M., Windebank, A., and Pandit, A. The effect of laminin peptide gradient in enzymatically cross-linked collagen scaffolds on neurite growth. J Biomed Mater Res A, 2010. **92A**(2): p. 484-492.
9. Shoichet, M.S., Tator, C.H., Poon, P., Kang, C., and Baumann, M.D. Intrathecal drug delivery strategy is safe and efficacious for localized delivery to the spinal cord. Prog Brain Res, 2007. **161**: p. 385-92.
10. Kang, C.E., Poon, P.C., Tator, C.H., and Shoichet, M.S. A new paradigm for local and sustained release of therapeutic molecules to the injured spinal cord for neuroprotection and tissue repair. Tissue Eng Part A, 2009. **15**(3): p. 595-604.
11. Gupta, D., Tator, C.H., and Shoichet, M.S. Fast-gelling injectable blend of hyaluronan and methylcellulose for intrathecal, localized delivery to the injured spinal cord. Biomaterials, 2006. **27**(11): p. 2370-9.
12. Gros, T., Sakamoto, J.S., Blesch, A., Havton, L.A., and Tuszynski, M.H. Regeneration of long-tract axons through sites of spinal cord injury using templated agarose scaffolds. Biomaterials, 2010. **31**(26): p. 6719-29.
13. Willerth, S.M., Faxel, T.E., Gottlieb, D.I., and Sakiyama-Elbert, S.E. The effects of soluble growth factors on embryonic stem cell differentiation inside of fibrin scaffolds. Stem Cells, 2007. **25**(9): p. 2235-44.
14. Phillips, J.B., King, V.R., Ward, Z., Porter, R.A., Priestley, J.V., and Brown, R.A. Fluid shear in viscous fibronectin gels allows aggregation of fibrous materials for CNS tissue engineering. Biomaterials, 2004. **25**(14): p. 2769-79.

15. Nomura, H., Zahir, T., Kim, H., Katayama, Y., Kulbatski, I., Morshead, C.M., Shoichet, M.S., and Tator, C.H. Extramedullary chitosan channels promote survival of transplanted neural stem and progenitor cells and create a tissue bridge after complete spinal cord transection. Tissue Eng Part A, 2008. **14**(5): p. 649-65.

16. Nomura, H., Baladie, B., Katayama, Y., Morshead, C.M., Shoichet, M.S., and Tator, C.H. Delayed implantation of intramedullary chitosan channels containing nerve grafts promotes extensive axonal regeneration after spinal cord injury. Neurosurgery, 2008. **63**(1): p. 127-41.

17. Dadsetan, M., Szatkowski, J.P., Yaszemski, M.J., and Lu, L. Characterization of photo-cross-linked oligo[poly(ethylene glycol) fumarate] hydrogels for cartilage tissue engineering. Biomacromolecules, 2007. **8**(5): p. 1702-9.

18. Tsai, E.C., Dalton, P.D., Shoichet, M.S., and Tator, C.H. Matrix inclusion within synthetic hydrogel guidance channels improves specific supraspinal and local axonal regeneration after complete spinal cord transection. Biomaterials, 2006. **27**(3): p. 519-33.

19. Chen, B.K., Knight, A.M., Madigan, N.N., Gross, L., Dadsetan, M., Nesbitt, J.J., Rooney, G.E., Currier, B.L., Yaszemski, M.J., Spinner, R.J., and Windebank, A.J. Comparison of polymer scaffolds in rat spinal cord: A step toward quantitative assessment of combinatorial approaches to spinal cord repair. Biomaterials, 2011. **32**(32): p. 8077-86.

20. Dadsetan, M., Knight, A.M., Lu, L., Windebank, A.J., and Yaszemski, M.J. Stimulation of neurite outgrowth using positively charged hydrogels. Biomaterials, 2009. **30**(23-24): p. 3874-81.

21. Franz, S., Weidner, N., and Blesch, A. Gene therapy approaches to enhancing plasticity and regeneration after spinal cord injury. Exp Neurol, 2012. **235**(1): p. 62-9.

22. McCall, J., Weidner, N., and Blesch, A. Neurotrophic factors in combinatorial approaches for spinal cord regeneration. Cell Tissue Res, 2012. **349**(1): p. 27-37.

23. Jain, A., McKeon, R.J., Brady-Kalnay, S.M., and Bellamkonda, R.V. Sustained delivery of activated Rho GTPases and BDNF promotes axon growth in CSPG-rich regions following spinal cord injury. PLoS One, 2011. **6**(1): p. e16135.

24. Mehrotra, S., Lynam, D., Liu, C., Shahriari, D., Lee, I., Tuszynski, M., Sakamoto, J., and Chan, C. Time controlled release of arabinofuranosylcytosine (Ara-C) from agarose hydrogels using layer-by-layer assembly: an in vitro study. J Biomater Sci Polym Ed, 2012. **23**(1-4): p. 439-63.

25. Pinzon, A., Calancie, B., Oudega, M., and Noga, B.R. Conduction of impulses by axons regenerated in a Schwann cell graft in the transected adult rat thoracic spinal cord. J Neurosci Res, 2001. **64**: p. 533-541.

26. Oudega, M., Moon, L.D., and de Almeida Leme, R.J. Schwann cells for spinal cord repair. Braz J Med Biol Res, 2005. **38**(6): p. 825-35.

27. Chen, B.K., Knight, A.M., de Ruiter, G.C., Spinner, R.J., Yaszemski, M.J., Currier, B.L., and Windebank, A.J. Axon regeneration through scaffold into distal spinal cord after transection. J Neurotrauma, 2009. **26**(10): p. 1759-71.

28. Biernaskie, J., Sparling, J.S., Liu, J., Shannon, C.P., Plemel, J.R., Xie, Y., Miller, F.D., and Tetzlaff, W. Skin-derived precursors generate myelinating

Schwann cells that promote remyelination and functional recovery after contusion spinal cord injury. J Neurosci, 2007. **27**(36): p. 9545-59.

29. Tabesh, H., Amoabediny, G., Nik, N.S., Heydari, M., Yosefifard, M., Siadat, S.O., and Mottaghy, K. The role of biodegradable engineered scaffolds seeded with Schwann cells for spinal cord regeneration. Neurochem Int, 2009. **54**(2): p. 73-83.
30. Wright, K.T., El Masri, W., Osman, A., Chowdhury, J., and Johnson, W.E. Concise review: Bone marrow for the treatment of spinal cord injury: mechanisms and clinical applications. Stem Cells, 2011. **29**(2): p. 169-78.
31. Ritfeld, G.J., Nandoe Tewarie, R.D., Vajn, K., Rahiem, S.T., Hurtado, A., Wendell, D.F., Roos, R.A., and Oudega, M. Bone marrow stromal cell-mediated tissue sparing enhances functional repair after spinal cord contusion in adult rats. Cell Ttransplant, 2012. **21**(7): p. 1561-75.
32. Caplan, A.I. and Dennis, J.E. Mesenchymal stem cells as trophic mediators. J Cell Biochem, 2006. **98**(5): p. 1076-84.
33. Chopp, M. and Li, Y. Treatment of neural injury with marrow stromal cells. Lancet Neurol, 2002. **1**(2): p. 92-100.
34. Li, Y., McIntosh, K., Chen, J., Zhang, C., Gao, Q., Borneman, J., Raginski, K., Mitchell, J., Shen, L., Zhang, J., Lu, D., and Chopp, M. Allogeneic bone marrow stromal cells promote glial-axonal remodeling without immunologic sensitization after stroke in rats. Exp Neurol, 2006. **198**(2): p. 313-25.
35. Li, Y., Chen, J., and Chopp, M. Adult bone marrow transplantation after stroke in adult rats. Cell Transplant, 2001. **10**(1): p. 31-40.
36. Chen, J., Li, Y., Katakowski, M., Chen, X., Wang, L., Lu, D., Lu, M., Gautam, S.C., and Chopp, M. Intravenous bone marrow stromal cell therapy reduces

apoptosis and promotes endogenous cell proliferation after stroke in female rat. J Neurosci Res, 2003. **73**(6): p. 778-86.

37. Caplan, A.I. Why are MSCs therapeutic? New data: new insight. J Pathol, 2009. **217**(2): p. 318-24.

38. Lu, P., Jones, L.L., and Tuszynski, M.H. BDNF-expressing marrow stromal cells support extensive axonal growth at sites of spinal cord injury. Exp Neurol, 2005. **191**(2): p. 344-60.

39. Rooney, G.E. Investigating the Neural Differentiation Potential of Mesenchymal Stem Cells, 2007, Regenerative Medicine Institute, National University of Ireland, Galway. p. 245.

40. Rooney, G.E., McMahon, S.S., Ritter, T., Garcia, Y., Moran, C., Madigan, N.N., Fluegel, A., Dockery, P., O'Brien, T., Howard, L., Windebank, A.J., and Barry, F. Neurotrophic Factor-Expressing Mesenchymal Stem Cells Survive Transplantation into the Contused Spinal Cord without Differentiating into Neural Cells. Tissue Eng Part A, 2009. **15**(10): p. 3049-3059.

41. Olson, H.E., Rooney, G.E., Gross, L., Nesbitt, J.J., Galvin, K.E., Knight, A., Chen, B., Yaszemski, M.J., and Windebank, A.J. Neural Stem Cell- and Schwann Cell-Loaded Biodegradable Polymer Scaffolds Support Axonal Regeneration in the Transected Spinal Cord. Tissue Eng Part A, 2009: p. 1797-1805.

42. Krych, A.J., Rooney, G.E., Chen, B., Schermerhorn, T.C., Ameenuddin, S., Gross, L., Moore, M.J., Currier, B.L., Spinner, R.J., Friedman, J.A., Yaszemski, M.J., and Windebank, A.J. Relationship between scaffold channel diameter and number of regenerating axons in the transected rat spinal cord. Acta Biomater, 2009. **5**(7): p. 2551-9.

43. Rooney, G.E., Knight, A.M., Madigan, N.N., Gross, L., Chen, B., Giraldo, C.V., Seo, S., Nesbitt, J.J., Dadsetan, M., Yaszemski, M.J., and Windebank, A.J. Sustained delivery of dibutyryl cyclic adenosine monophosphate to the transected spinal cord via oligo [(polyethylene glycol) fumarate] hydrogels. Tissue Eng Part A, 2011. **17**(9-10): p. 1287-302.

44. Rooney, G.E., Moran, C., McMahon, S.S., Ritter, T., Maenz, M., Flugel, A., Dockery, P., O'Brien, T., Howard, L., Windebank, A.J., and Barry, F.P. Gene-modified mesenchymal stem cells express functionally active nerve growth factor on an engineered poly lactic glycolic acid (PLGA) substrate. Tissue Eng Part A, 2008. **14**(5): p. 681-90.

45. Jaiswal, N., Haynesworth, S.E., Caplan, A.I., and Bruder, S.P. Osteogenic differentiation of purified, culture-expanded human mesenchymal stem cells in vitro. J Cell Biochem, 1997. **64**(2): p. 295-312.

46. Petit, B., Masuda, K., D'Souza, A.L., Otten, L., Pietryla, D., Hartmann, D.J., Morris, N.P., Uebelhart, D., Schmid, T.M., and Thonar, E.J. Characterization of crosslinked collagens synthesized by mature articular chondrocytes cultured in alginate beads: comparison of two distinct matrix compartments. Exp Cell Res, 1996. **225**(1): p. 151-61.

47. Jo, S., Engel, P.S., and Mikos, A.G. Synthesis of poly(ethylene glycol)-tethered poly(propylene fumarate) and its modification with GRGD peptide. Polymer, 2000. **41**: p. 7595-7604.

48. National Academy of Sciences, I.f.L.A.R. Guide for the Care and Use of Laboratory Animals, Earth and Life Sciences, N.R.C., Editor 2010, The National Academies Press, Washington DC. p. 1-218.

49. Basso, D.M., Beattie, M.S., and Bresnahan, J.C. A sensitive and reliable locomotor rating scale for open field testing in rats. J Neurotrauma, 1995. **12**: p. 1-21.

50. Lyck, L., Dalmau, I., Chemnitz, J., Finsen, B., and Schroder, H.D. Immunohistochemical markers for quantitative studies of neurons and glia in human neocortex. J Histochem Cytochem, 2008. **56**(3): p. 201-21.

51. Hol, E.M., Roelofs, R.F., Moraal, E., Sonnemans, M.A., Sluijs, J.A., Proper, E.A., de Graan, P.N., Fischer, D.F., and van Leeuwen, F.W. Neuronal expression of GFAP in patients with Alzheimer pathology and identification of novel GFAP splice forms. Mol Psychiatry, 2003. **8**(9): p. 786-96.

52. Hornigold, N., Craven, R.A., Keen, J.N., Johnson, T., Banks, R.E., and Mooney, A.F. Upregulation of Hic-5 in glomerulosclerosis and its regulation of mesangial cell apoptosis. Kidney Int. **77**(4): p. 329-38.

53. Barnes, C.A., Brison, J., Michel, R., Brown, B.N., Castner, D.G., Badylak, S.F., and Ratner, B.D. The surface molecular functionality of decellularized extracellular matrices. Biomaterials, 2011. **32**(1): p. 137-43.

54. Feldman, A.L., Arber, D.A., Pittaluga, S., Martinez, A., Burke, J.S., Raffeld, M., Camos, M., Warnke, R., and Jaffe, E.S. Clonally related follicular lymphomas and histiocytic/dendritic cell sarcomas: evidence for transdifferentiation of the follicular lymphoma clone. Blood, 2008. **111**(12): p. 5433-9.

55. Henwood, A.F. The application of heated detergent dewaxing and rehydration to immunohistochemistry. Biotech Histochem, 2010. **87**(1): p. 46-50.

56. Howard, C.V., Reed, M.G. Unbiased Stereology, Three Dimensional Measurement in Microscopy. 2nd ed2010, Liverpool: QTP Publications.

57. Garcia, Y., Breen, A., Burugapalli, K., Dockery, P., and Pandit, A. Stereological methods to assess tissue response for tissue-engineered scaffolds. Biomaterials, 2007. **28**(2): p. 175-86.

58. Dockery, P. and Fraher, J. The quantification of vascular beds: a stereological approach. Exp Mol Pathol, 2007. **82**(2): p. 110-20.

59. Jakubovsky, J., Guller, L., Cerna, M., Balazova, K., Polak, S., Jakubovska, V., and Babal, P. Fluorescence of hematoxylin and eosin-stained histological sections of the human spleen. Acta Histochem, 2002. **104**(4): p. 353-6.

60. Baron-Van Evercooren, A., Clerin-Duhamel, E., Lapie, P., Gansmuller, A., Lachapelle, F., and Gumpel, M. The fate of Schwann cells transplanted in the brain during development. Dev Neurosci, 1992. **14**(2): p. 73-84.

61. Afshari, F.T., Kwok, J.C., and Fawcett, J.W. Analysis of Schwann-astrocyte interactions using in vitro assays. J Vis Exp, 2011(47): p. doi:pii: 2214.

62. Lakatos, A., Franklin, R.J., and Barnett, S.C. Olfactory ensheathing cells and Schwann cells differ in their in vitro interactions with astrocytes. Glia, 2000. **32**(3): p. 214-25.

63. Afshari, F.T., Kwok, J.C., White, L., and Fawcett, J.W. Schwann cell migration is integrin-dependent and inhibited by astrocyte-produced aggrecan. Glia. **58**(7): p. 857-69.

64. Santos-Silva, A., Fairless, R., Frame, M.C., Montague, P., Smith, G.M., Toft, A., Riddell, J.S., and Barnett, S.C. FGF/heparin differentially regulates Schwann cell and olfactory ensheathing cell interactions with astrocytes: a role in astrocytosis. J Neurosci, 2007. **27**(27): p. 7154-67.

65. Lavdas, A.A., Papastefanaki, F., Thomaidou, D., and Matsas, R. Schwann cell transplantation for CNS repair. Curr Med Chem, 2008. **15**(2): p. 151-60.

66. Lavdas, A.A., Chen, J., Papastefanaki, F., Chen, S., Schachner, M., Matsas, R., and Thomaidou, D. Schwann cells engineered to express the cell adhesion molecule L1 accelerate myelination and motor recovery after spinal cord injury. Exp Neurol, 2010. **221**(1): p. 206-16.

67. Lavdas, A.A., Papastefanaki, F., Thomaidou, D., and Matsas, R. Cell adhesion molecules in gene and cell therapy approaches for nervous system repair. Curr Gene Ther, 2011. **11**(2): p. 90-100.

68. Bushong, E.A., Martone, M.E., and Ellisman, M.H. Examination of the relationship between astrocyte morphology and laminar boundaries in the molecular layer of adult dentate gyrus. J Comp Neurol, 2003. **462**(2): p. 241-51.

69. Laywell, E.D., Dorries, U., Bartsch, U., Faissner, A., Schachner, M., and Steindler, D.A. Enhanced expression of the developmentally regulated extracellular matrix molecule tenascin following adult brain injury. Proc Natl Acad Sci U S A, 1992. **89**(7): p. 2634-8.

70. Steindler, D.A. Glial boundaries in the developing nervous system. Annu Rev Neurosci, 1993. **16**: p. 445-70.

71. Chan-Ling, T., Chu, Y., Baxter, L., Weible Ii, M., and Hughes, S. In vivo characterization of astrocyte precursor cells (APCs) and astrocytes in developing rat retinae: differentiation, proliferation, and apoptosis. Glia, 2009. **57**(1): p. 39-53.

72. Jessen, K.R. and Mirsky, R. The origin and development of glial cells in peripheral nerves. Nature reviews. Neuroscience, 2005. **6**(9): p. 671-82.

73. Nagoshi, N., Shibata, S., Hamanoue, M., Mabuchi, Y., Matsuzaki, Y., Toyama, Y., Nakamura, M., and Okano, H. Schwann cell plasticity after

spinal cord injury shown by neural crest lineage tracing. Glia, 2011. **59**(5): p. 771-84.

74. Feigin, I. and Ogata, J. Schwann cells and peripheral myelin within human central nervous tissues: the mesenchymal character of Schwann cells. J Neuropathol Exp Neurol, 1971. **30**(4): p. 603-12.

75. Beattie, M.S., Bresnahan, J.C., Komon, J., Tovar, C.A., Van Meter, M., Anderson, D.K., Faden, A.I., Hsu, C.Y., Noble, L.J., Salzman, S., and Young, W. Endogenous repair after spinal cord contusion injuries in the rat. Exp Neurol, 1997. **148**(2): p. 453-63.

76. Laylor, R., Dewchand, H., Simpson, E., and Dazzi, F. Engraftment of allogeneic hematopoietic stem cells requires both inhibition of host-versus-graft responses and 'space' for homeostatic expansion. Transplantation, 2005. **79**(11): p. 1484-91.

77. Griffiths, I.R. Spinal cord blood flow after acute experimental cord injury in dogs. J Neurol Sci, 1976. **27**(2): p. 247-59.

78. Bao, F. and Liu, D. Peroxynitrite generated in the rat spinal cord induces neuron death and neurological deficits. Neuroscience, 2002. **115**(3): p. 839-49.

79. Braughler, J.M. and Hall, E.D. Involvement of lipid peroxidation in CNS injury. J Neurotrauma, 1992. **9 Suppl 1**: p. S1-7.

80. Brundin, P., Karlsson, J., Emgard, M., Schierle, G.S., Hansson, O., Petersen, A., and Castilho, R.F. Improving the survival of grafted dopaminergic neurons: a review over current approaches. Cell Transplant, 2000. **9**(2): p. 179-95.

81. Pearse, D.D., Sanchez, A.R., Pereira, F.C., Andrade, C.M., Puzis, R., Pressman, Y., Golden, K., Kitay, B.M., Blits, B., Wood, P.M., and Bunge,

M.B. Transplantation of Schwann cells and/or olfactory ensheathing glia into the contused spinal cord: Survival, migration, axon association, and functional recovery. Glia, 2007. **55**(9): p. 976-1000.

82. Chopp, M., Zhang, X.H., Li, Y., Wang, L., Chen, J., Lu, D., Lu, M., and Rosenblum, M. Spinal cord injury in rat: treatment with bone marrow stromal cell transplantation. Neuroreport, 2000. **11**(13): p. 3001-5.

83. Hofstetter, C.P., Schwarz, E.J., Hess, D., Widenfalk, J., El Manira, A., Prockop, D.J., and Olson, L. Marrow stromal cells form guiding strands in the injured spinal cord and promote recovery. Proc Natl Acad Sci U S A, 2002. **99**(4): p. 2199-204.

84. Wu, S., Suzuki, Y., Ejiri, Y., Noda, T., Bai, H., Kitada, M., Kataoka, K., Ohta, M., Chou, H., and Ide, C. Bone marrow stromal cells enhance differentiation of cocultured neurosphere cells and promote regeneration of injured spinal cord. J Neurosci Res, 2003. **72**: p. 343-351.

85. Ankeny, D.P., McTigue, D.M., and Jakeman, L.B. Bone marrow transplants provide tissue protection and directional guidance for axons after contusive spinal cord injury in rats. Exp Neurol, 2004. **190**(1): p. 17-31.

86. Himes, B.T., Neuhuber, B., Coleman, C., Kushner, R., Swanger, S.A., Kopen, G.C., Wagner, J., Shumsky, J.S., and Fischer, I. Recovery of function following grafting of human bone marrow-derived stromal cells into the injured spinal cord. Neurorehabil Neural Repair, 2006. **20**(2): p. 278-96.

87. Vaquero, J., Zurita, M., Oya, S., and Santos, M. Cell therapy using bone marrow stromal cells in chronic paraplegic rats: systemic or local administration? Neurosci Lett, 2006. **398**(1-2): p. 129-34.

88. Zurita, M. and Vaquero, J. Bone marrow stromal cells can achieve cure of chronic paraplegic rats: functional and morphological outcome one year after transplantation. Neurosci Lett, 2006. **402**(1-2): p. 51-6.

89. Sykova, E., Jendelova, P., Urdzikova, L., Lesny, P., and Hejcl, A. Bone marrow stem cells and polymer hydrogels--two strategies for spinal cord injury repair. Cell Mol Neurobiol, 2006. **26**(7-8): p. 1113-29.

90. Hejcl, A., Sedy, J., Kapcalova, M., Toro, D.A., Amemori, T., Lesny, P., Likavcanova-Masinova, K., Krumbholcova, E., Pradny, M., Michalek, J., Burian, M., Hajek, M., Jendelova, P., and Sykova, E. HPMA-RGD hydrogels seeded with mesenchymal stem cells improve functional outcome in chronic spinal cord injury. Stem Cells Dev, 2010. **19**(10): p. 1535-46.

91. Zeng, X., Zeng, Y.S., Ma, Y.H., Lu, L.Y., Du, B.L., Zhang, W., Li, Y., and Chan, W.Y. Bone marrow mesenchymal stem cells in a three-dimensional gelatin sponge scaffold attenuate inflammation, promote angiogenesis, and reduce cavity formation in experimental spinal cord injury. Cell Transplant 2011. **20**(11-12): p. 1881-99.

92. Crisan, M., Deasy, B., Gavina, M., Zheng, B., Huard, J., Lazzari, L., and Peault, B. Purification and long-term culture of multipotent progenitor cells affiliated with the walls of human blood vessels: myoendothelial cells and pericytes. Methods Cell Biol, 2008. **86**: p. 295-309.

93. Caplan, A.I. All MSCs are pericytes? Cell Stem Cell, 2008. **3**(3): p. 229-30.

94. da Silva Meirelles, L., Caplan, A.I., and Nardi, N.B. In search of the in vivo identity of mesenchymal stem cells. Stem Cells, 2008. **26**(9): p. 2287-99.

95. Augello, A., Kurth, T.B., and De Bari, C. Mesenchymal stem cells: a perspective from in vitro cultures to in vivo migration and niches. Eur Cell Mater, 2010. **20**: p. 121-33.

96. Takashima, Y., Era, T., Nakao, K., Kondo, S., Kasuga, M., Smith, A.G., and Nishikawa, S. Neuroepithelial cells supply an initial transient wave of MSC differentiation. Cell, 2007. **129**(7): p. 1377-88.

97. Frank, R.N., Dutta, S., and Mancini, M.A. Pericyte coverage is greater in the retinal than in the cerebral capillaries of the rat. Invest Ophthalmol Vis Sci, 1987. **28**(7): p. 1086-91.

98. Shepro, D. and Morel, N.M. Pericyte physiology. Faseb J, 1993. **7**(11): p. 1031-8.

99. Kamouchi, M., Ago, T., Kuroda, J., and Kitazono, T. The possible roles of brain pericytes in brain ischemia and stroke. Cell Mol Neurobiol, 2012. **32**(2): p. 159-65.

100. Yamashima, T., Tonchev, A.B., Vachkov, I.H., Popivanova, B.K., Seki, T., Sawamoto, K., and Okano, H. Vascular adventitia generates neuronal progenitors in the monkey hippocampus after ischemia. Hippocampus, 2004. **14**(7): p. 861-75.

101. Ohab, J.J., Fleming, S., Blesch, A., and Carmichael, S.T. A neurovascular niche for neurogenesis after stroke. J Neurosci, 2006. **26**(50): p. 13007-16.

102. Oudega, M. Molecular and cellular mechanisms underlying the role of blood vessels in spinal cord injury and repair. Cell Tissue Res, 2012. **349**(1): p. 269-88.

FIGURE LEGENDS

FIG. 1. Positively-charged OPF scaffolds were loaded with Matrigel, Schwann cells, or eGFP-MSCs, surgically implanted into a T9 complete spinal cord transection (n=6 per animal group) and were analysed histologically as individual channels. **(A)** Fluorescent eGFP-MSCs within OPF^{+} scaffold channels following cell loading 238,000 cells per scaffold. **(B)** Implanted polymer scaffolds were aligned and integrated between the transected ends of the spinal cord, conveying cables of tissue growth at four weeks. **(C)** The overall architecture of the scaffold was preserved following tissue sectioning. The mean cross sectional area for Matrigel channels (120,990 +/- 1806 μm^2) ($p<0.001$), and Schwann cell channels (114,264 +/- 2363 μm^2)($p<0.01$) was higher than eGFP-MSC channels (106,691 +/- 1677 μm^2) post fixation. **(D-E)** Eosin autofluorence of representative Matrigel, Schwann Cell and eGFP-MSC channels (left to right). **(G-H)** Axonal neurofilament protein was visualized with antibody staining and the DAB chromogen (dark brown) in Matrigel, Schwann Cell and eGFP-MSC channels (left to right). **(J-L)** Collagen IV antibody staining (green) identified blood vessels in Matrigel, Schwann cell and eGFP-MSC channels (left to right).

FIG. 2. The cellular composition of scaffold channels was identified with antibodies to Glial Fibrillary Acid Protein (GFAP) (orange) and the S-100 antigen (green) in Matrigel **(A)**, and Schwann cell channels at 20 x magnification **(B)** and 60 x magnification **(C)**. **(D)** GFAP (orange) and eGFP-MSC fluorescence (green) was counterstained with DAPI (blue) in Z-stacked imaging of an eGFP-MSC channel.

eGFP-MSC fluorescence (green). eGFP MSCs at 40 x magnification **(E**) confirmed cellular viability.

FIG. 3. (A) Mean proportional channel area occupied by GFAP, S-100 and eGFP positive cells in each animal group (n=91 Matrigel, 70 Schwann cell and 72 eGFP-MSC channels). A significantly higher proportion of GFAP staining was seen in the Matrigel group ($p<0.001$). **(B)** Median axon counts in Matrigel, Schwann cell and eGFP-MSC scaffolds (n=6). Each point represents the sum of axon counts at a quarter length interval through a scaffold.

FIG. 4. Axons were identified in the channel core by Neurofilament staining in Matrigel, Schwann Cell and eGFP-MSC channels (A-C). Blood vessels were identified using staining to Collagen IV (D-F).

FIG. 5. Unbiased stereology estimates for blood vessel volume **(A)**, total blood vessel length **(B)**, and vessel surface area **(C)** in Matrigel (n=93), Schwann cell (n=86) and eGFP-MSC (n=91) channel sections. Mean vessel cross sectional areas in each animal group **(D)** were calculated from the fractional volume, length and surface area estimates. Estimates for vessel radial diffusion **(E)** were calculated as inversely proportional to the fractional length volume. Total axon number, in Matrigel and Schwann cell groups combined (at n=28 quarter length scaffold intervals), negatively correlated to the mean radial diffusion distance as a hyperbolic function **(F)**.

Figure 1

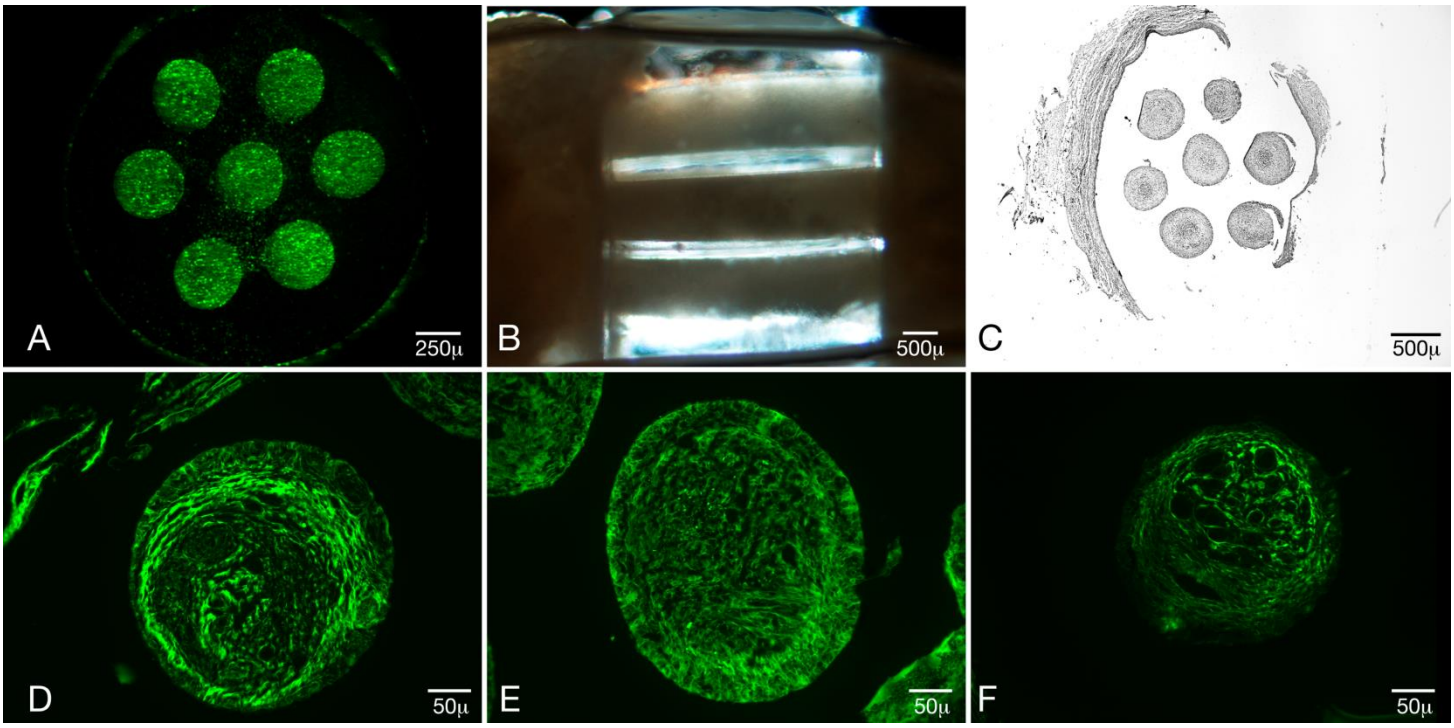

Figure 2

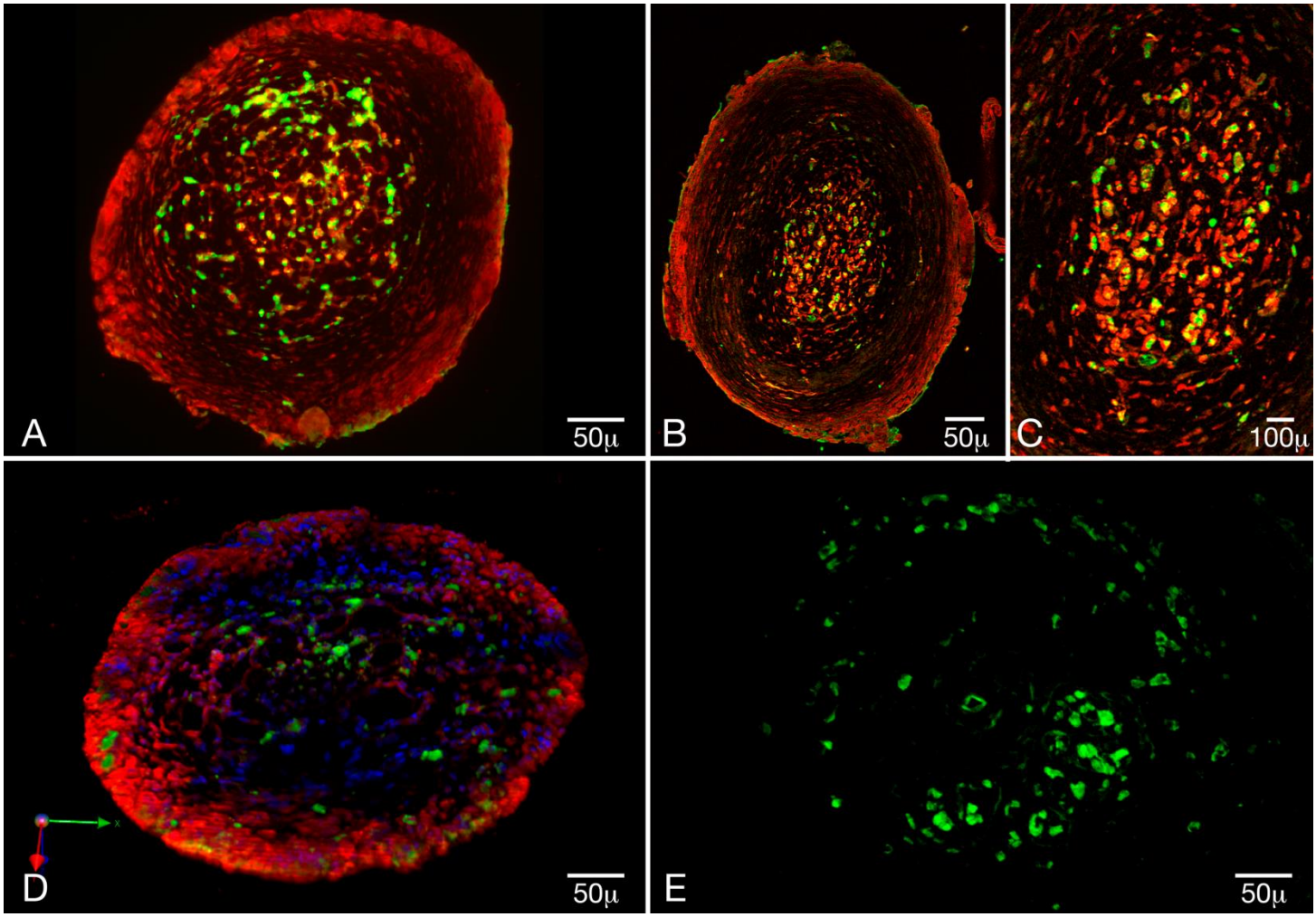

Figure 3

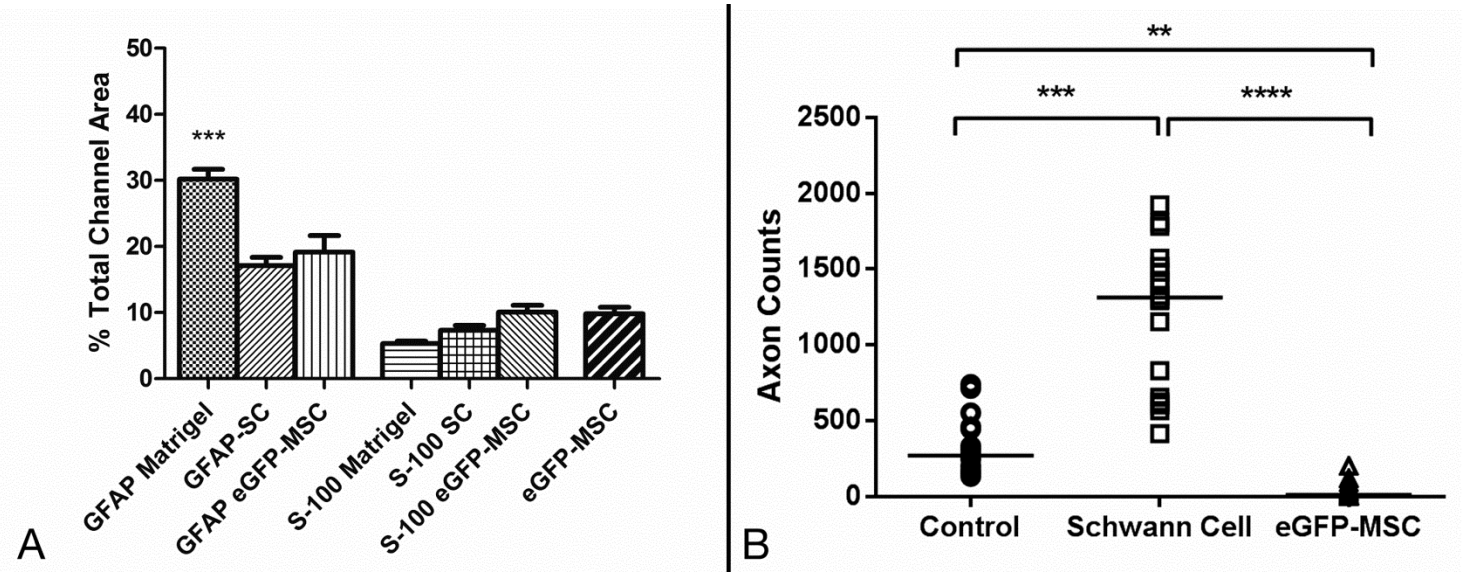
A
% Total Channel Area
50
40
30
20
10
0
***
GFAP Matrigel
GFAP-SC
GFAP eGFP-MSC
S-100 Matrigel
S-100 SC
S-100 eGFP-MSC
eGFP-MSC
B
**
***
****
Axon Counts
2500
2000
1500
1000
500
0
Control
Schwann Cell
eGFP-MSC

Figure 4

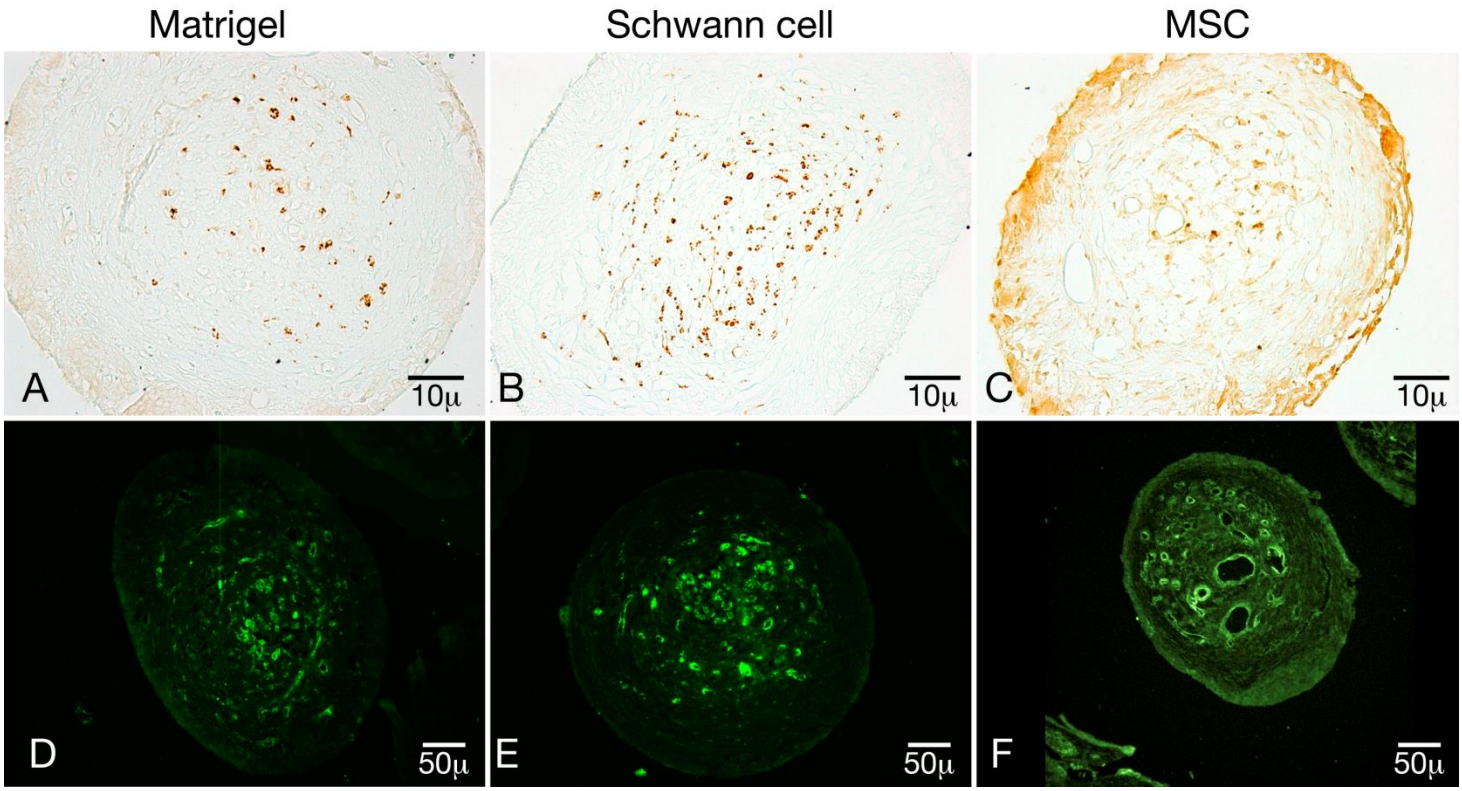

Figure 5

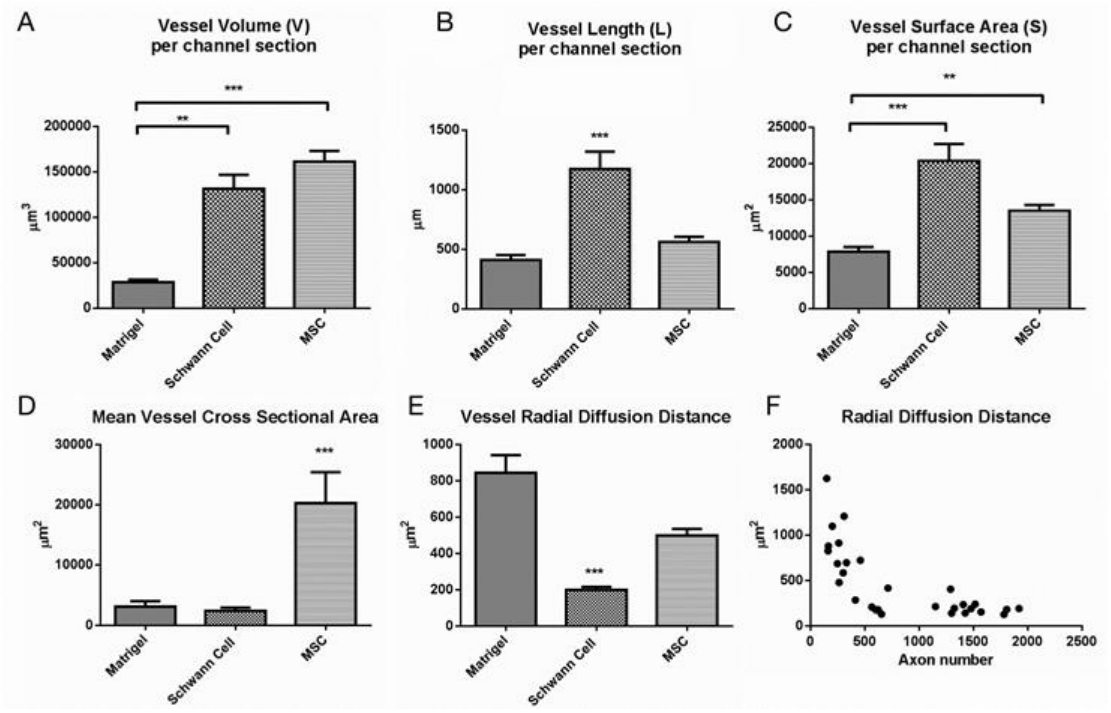
A
Vessel Volume (V)
per channel section
μm³
200000
150000
100000
50000
0
***
**
Matrigel
Schwann Cell
MSC
B
Vessel Length (L)
per channel section
μm
1500
1000
500
0
***
Matrigel
Schwann Cell
MSC
C
Vessel Surface Area (S)
per channel section
μm²
25000
20000
15000
10000
5000
0
**
***
Matrigel
Schwann Cell
MSC
D
Mean Vessel Cross Sectional Area
μm²
30000
20000
10000
0
***
Matrigel
Schwann Cell
MSC
E
Vessel Radial Diffusion Distance
μm²
1000
800
600
400
200
0
***
Matrigel
Schwann Cell
MSC
F
Radial Diffusion Distance
μm²
2000
1500
1000
500
0
0
500
1000
1500
2000
2500
Axon number